Check for updates

Electrochemical Sensing with Spatially Patterned Pt Octahedra Electrodes

Dirk Jonker, Cavit Eyovge, Erwin Berenschot, Valerio Di Palma, Dorothee Wasserberg, Sandra Michel-Souzy, Pascal Jonkheijm, Silke Krol, Han Gardeniers, Mariadriana Creatore, Niels Tas,* and Arturo Susarrey-Arce**

Locally controlling the position of electrodes in 3D can open new avenues to collect electrochemical signals in complex sensing environments. Implementing such electrodes via an electrical network requires advanced fabrication approaches. This work uses corner lithography and Pt ALD to produce electrochemical 3D electrodes. The approach allows the fabrication of (sub)micrometer size Pt octahedra electrodes spatially supported over 3D fractal-like structures. As a proof of concept, electrochemical sensing of ferrocyanide in biofouling environments, e.g., bovine serum albumin (BSA) and *Pseudomonas aeruginosa* (*P. aeruginosa*), is assessed. Differences between before and after BSA addition show a reduction in the active electrode surface area (ΔA_{eff}) ≈49% ± 7% for the flat electrode. In comparison, a ΔA_{eff} reduction of 25% ± 2% for the 3D electrode has been found. The results are accompanied by a 24% ± 16% decrease in peak current for the flat Pt substrate and a 14% ± 5% decrease in peak current for the 3D electrode 24 h after adding BSA. In the case of *P. aeruginosa*, the 3D electrode retains electrochemical signals, while the flat electrode does not. The results demonstrate that the 3D Pt electrodes are more stable than their flat counterparts under biofouling conditions.

1. Introduction

Advances in fabrication technology enable the production of artificially engineered geometries of arbitrary shape with desired functionalities, such as low-weight structures with increased mechanical strength,[1] plasmonic structures for sensing,[2] light-emitting structures for light management in optoelectronics,[3,4] scaffold-like structures to direct cell growth[5–9] and structured electrochemical systems for high energy storage and conversion.[10–12] The cited work shares a similar endowment in terms of multiscale fabrication of geometrical architectures, typically accomplished using micro(nano)fabrication[13,14] or additive manufacturing (AM).[15,16]

AM methods, such as two-photon lithography, have been proven quite effective in reaching micrometer resolution precision to form local polymeric and composite patterns in space.[17,18] However, obtaining multi-material combinations, such as metal and insulating constituents, is still in the early stages. Currently, AM allows single-metal production of 3D structures when combined with other approaches, such as Cu electrodeposition.[19–21] Like Cu, noble metals such as Au and Pt are not trivial to pattern in 3D. However, Au and Pt remain the metals of choice for electrochemical sensing due to their

D. Jonker, C. Eyovge, E. Berenschot, S. Krol, H. Gardeniers, N. Tas, A. Susarrey-Arce
Mesoscale Chemical Systems
MESA+ Institute
University of Twente
Drienerlolaan 5, Enschede 7522 NB, The Netherlands
E-mail: d.jonker@utwente.nl; n.r.tas@utwente.nl; a.susarreyarce@utwente.nl

The ORCID identification number(s) for the author(s) of this article can be found under https://doi.org/10.1002/admt.202300878

© 2024 The Authors. Advanced Materials Technologies published by Wiley-VCH GmbH. This is an open access article under the terms of the Creative Commons Attribution License, which permits use, distribution and reproduction in any medium, provided the original work is properly cited.

DOI: 10.1002/admt.202300878

V. Di Palma, M. Creatore
Department of Applied Physics and Science of Education
Eindhoven University of Technology
Eindhoven 5600 MB, The Netherlands

D. Wasserberg, S. Michel-Souzy, P. Jonkheijm
Department of Molecules and Materials
Faculty of Science and Technology
MESA+ Institute and TechMed Centre
University of Twente
P.O. Box 217, Enschede 7500 AE, The Netherlands

D. Wasserberg
LipoCoat B.V.
Hengelosestraat 541, Enschede 7521 AG, The Netherlands

S. Krol
Encytos B.V.
Piet Heinstraat 12, Enschede 7511 JE, The Netherlands

inertness and low toxicity, particularly in biological environments,[22] e.g., metal foams known for their 3D porous network.[23,24]

Although 3D porous networks have been fabricated, a missing link is the spatial control of metals to produce structures of high hierarchy capable of recording specific electrochemical signals in complex cellular environments.[22] A way forward is using micro(nano)fabrication methods to pave the path for producing multi-material patterns, as in the case of support matrixes, to allocate metallic features that function as microelectrodes. Such a proposition might require the use of multiple materials during fabrication. Multimaterial layered patterns of asymmetric metal electrodes can be constructed using adhesion lithography.[14,25] The advantage of adhesion lithography is that it can overcome the limitations of electron-beam lithography regarding scalability and material combinations. Another lithographic method is selective passivation, which involves depositing a protective layer on 3D microelectrodes using polydopamine electrodeposition and local laser ablation. This method enables the fabrication of complex electrode patterns.[26] However, chemical methods should not be disregarded because they can also lead to the formation of 3D structures for electrochemistry. Depending on the material construct, the method might involve more than one step. For example, anodization can produce porous alumina, which creates honeycomb-like structures within the alumina.[27] The resulting structures can then be used as a mold for metal deposition into the alumina pores. A well-ordered array of metal nanorods can then be grown within the alumina pores. Similar structures have been achieved using Talbot Lithography, which allows the fabrication of hollow Au-like rod structures.[2]

Among the fabrication methods mentioned above, we have identified that the spatial control of multi-material compositions is challenging. Recently, the fabrication of pillar-like structures decorated with metal features has been demonstrated. The fabrication method combines silicon lithography and metal casting,[13] which allows the creation of silicon-metal structures. Such a step is relevant as it opens the opportunity to produce optoelectronic and electrochemical functional devices with spatially distributed patterns, ideal for interrogating cellular environments locally.[28]

Another example of arrangements of metal electrodes for electric signal recording is patterned probes.[29,30] Tailoring probe geometries can increase accessibility to remote specimen areas to enable electrochemical recording. Alternatively, 3D-arranged electrical hierarchical structures can be constructed with channels and/or networks of pores. This asset can provide electrical recording and stability during electrochemical measurements, allowing ions and redox molecules to transport through channels or pores.[23,31] This is particularly relevant under (bio)fouling environments. Fouling environments form an impermeable layer on the electrode surface, effectively blocking it, which affects the electron-transfer reactions of the analyte molecules. Channels and pores can provide the additional advantage of allowing the diffusion of small molecules to the proximity of the electrode surface despite heavy fouling.[32,33] This example also includes application pathways for 3D geometries with local electrochemical readouts to improve the sensing of redox couples under fouling conditions.

Among the various hierarchical topographies dedicated to electrochemical sensing,[34] topographies inspired by nature can also be used to support metal patterning. This is the case with fractals. Fractals are known for their high level of organization, functional morphology, and similarity over a range of dimensional scales. Fractal concepts have been used in flat footprints,[35,36] fluidic channels,[35,37,38] and 3D printed structures.[39,40] Fractals have also been utilized to support photoactive materials,[41–43] optical elements,[44] or synthetic materials[45] such as hydrogels.[46–48] However, the use of fractal-like insulating geometries to support 3D arrangements of metal particles like octahedra is unexplored. The arrangement of 3D patterned fractal-like structures can distribute the electrical currents over specific positions in space.

This work introduces the fabrication of the 3D periodic arrangement of Pt octahedra in 3D over fractal-like geometries. An electrical connection to the Pt octahedra presented at the apices of the 3D fractal-like structures enables electrochemical recording, also known as 3D Pt electrodes. The fractal structures are produced using corner lithography and atomic layer deposition (ALD) of Pt. Fractal fabrication relies on silicon dioxide (SiO_2) growth and conformal stoichiometric silicon nitride (Si_3N_4) depositions in a silicon (Si) master mold containing the negative of the desired fractal geometry.[49] Corner lithography is a critical element in fractal fabrication, which forms sub-micron nozzles inside the mold, allowing the ALD Pt-precursor access. The structures are then back-bonded to a back-patterned electrical SiO_2 membrane for electrical connectivity. As a proof of concept, the functionality of the patterned Pt octahedra over the fractal network is assessed during the electrochemical recording of a redox molecule, here, ferrocyanide, under biofouling environments, e.g., BSA and *P. aeruginosa*. The results of under-fouling environments demonstrate that the 3D Pt electrodes permit the recording of electrochemical signals.

2. Results and Discussion

2.1. Fabrication of the 3D Platinum Electrodes

The goal of this section is to explain the deposition of Pt by ALD in the 3D fractal geometric mold. Additional processing returning in free-standing 3D fractal structures with partially exposed Pt electrodes is addressed. Furthermore, a strategy to fabricate contact electrodes that enable electrical contact between a 3D Pt fractal array and an electrical interface is presented.

The fabrication process of the 3D fractal is based on corner lithography and is elaborated upon elsewhere.[49,50] In short, iterations of thermal oxidation of silicon (100), patterning of the thermally grown silicon dioxide (t-SiO_2) layer by timed chemical wet-etching in hydrofluoric acid (HF), and timed anisotropic wet-etching of silicon in tetramethylammonium hydroxide (TMAH) leads to the formation of -at first- a pyramidal and -afterward- octahedral features with increasing iterations. For detailed information, see the section and Figure S1 (Supporting Information). This method largely relies on the usage of the retarded t-SiO_2 growth in concave corners, which can be further amplified by using silicon nitride-assisted local oxidation of silicon (LOCOS) (**Figure 1a**). The number of octahedral cavities in the 3D mold increases exponentially (5^{N-1}) together with the hierarchical order (N^{th} generation) after the initial pyramidal feature formation

© 2024 The Authors. Advanced Materials Technologies published by Wiley-VCH GmbH

2365709x, 0, Downloaded from https://onlinelibrary.wiley.com/doi/10.1002/admt.202300878 by University Of Twente Finance Department, Wiley Online Library on [18/01/2024]. See the Terms and Conditions (https://onlinelibrary.wiley.com/terms-and-conditions) on Wiley Online Library for rules of use; OA articles are governed by the applicable Creative Commons License

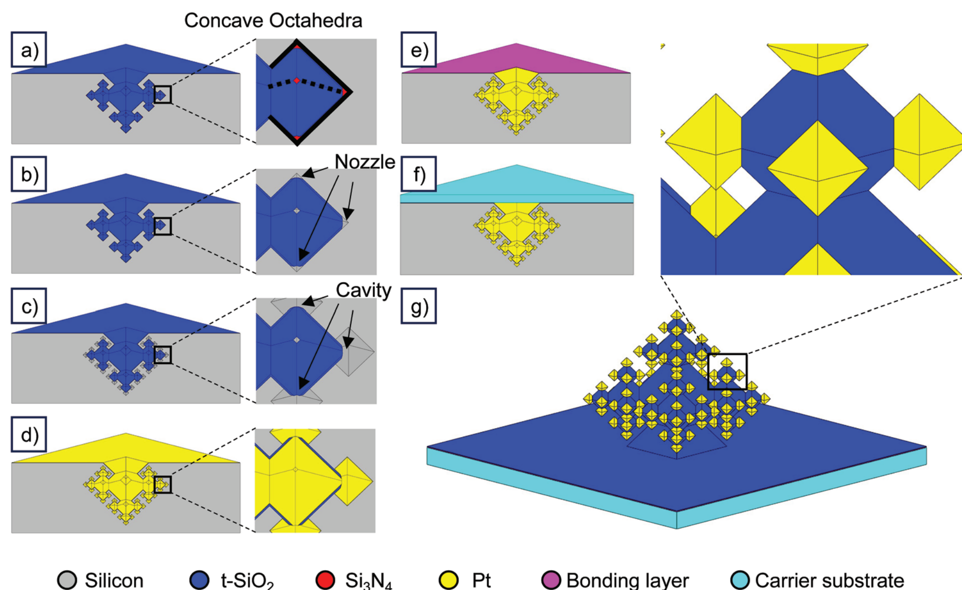

Figure 1. Schematic representation of the fabrication steps to create 3D Pt fractal electrodes. a) The process starts with a 3rd generation fractal mold featuring concave octahedral cavities. b) Selective wet chemical etching removes the nitride plug, resulting in 5^{N-1} t-SiO_2 nozzle ends. c) These nozzle ends are then used for an anisotropic wet-chemical etch of silicon, transforming the structure into a 4th generation fractal mold. d) Pt is conformally coated using Atomic Layer Deposition (ALD) on both the silicon substrate and the interior of the fractal mold. e) A bonding layer, whose composition and functionality are discussed further in Figure 3, *is* deposited and patterned. f) The substrate with the Pt-coated fractal mold is bonded to a 500 µm thick glass carrier substrate. g) The silicon mold is removed, revealing the free-standing 3D Pt fractal electrode.

(0th generation) and after every corner lithography iteration. An inherent feature of the corner lithography method is that every Nth iteration, after the 1st generation octahedral feature formation, is preceded by the formation of 5^{N-1} t-SiO_2 nozzle-like features, exposing Si at the nozzle ends (Figure 1b).[49,50] These nozzle-like features function as an internal hard mask for anisotropic wet-etching of Si to form the octahedral cavities (Figure 1c). However, to obtain the 3D Pt fractal electrode mold, the iterative cycle is stopped after anisotropic wet-etching of silicon and concluded with ALD of Pt in the 3D fractal mold (Figure 1d).

Adding a bonding layer stack (Figure 1e) enables bonding to a carrier wafer (Figure 1f) and making a connection to an electrical interface later on. Selective wet chemical etching of the silicon mold uncovers the free-standing 3D Pt fractal electrode (3D electrode) (Figure 1g). Considering Figure 1d,g, one could derive that while the Pt is presented on the exterior only at the 4th generation octahedra, the lower generation octahedra contains platinum on the interior and t-SiO_2 on the exterior. Thus, the platinum film can only be found to be interconnected across the whole structure, but an electrochemical interface is only intended at the outer octahedra.

The deposition of Pt is achieved using ALD. The optimized recipe used is reported in **Scheme 1** and methods section. An example of a deposited Pt layer is displayed using the 1st generation Si mold (Figure S1b, Supporting Information) with a nozzle width of 130 nm (**Figure 2**a,b). A thickness variation is observed across the flat and inclined surfaces (Figure S2, Supporting Information). The Pt film thickness on the flat surface is measured to be ≈30 nm, whereas the Pt and in the cavity of the Si mold is measured to be 25 ± 5 nm. A close look at Figure S2 (Supporting Information) shows an example of a non-uniform Pt layer with a thickness difference of ≈10 nm between the normal and inclined surfaces. The 1st generation 3D Pt electrode has a single Pt octahedron at the top (yellow color) and a t-SiO_2 base (blue color) (Figure 2c).

To explore the possibilities of the presented method, corner lithography in combination with ALD of Pt, anodic bonding to a carrier substrate, and sacrificial etching of Si have been carried out on higher-order structures. In Figure 2d–f, the fabrication of a 3rd generation 3D Pt electrode is shown, characterized by its network consisting of 25 outer Pt octahedra with edge lengths of ≈1 µm (bright color, highlighted with a yellow arrow). From the scanning electron microscopy (SEM) image, the Pt octahedra appears to be smooth, and thickness uniformities are observed throughout the concave cavities, both for the lower and higher

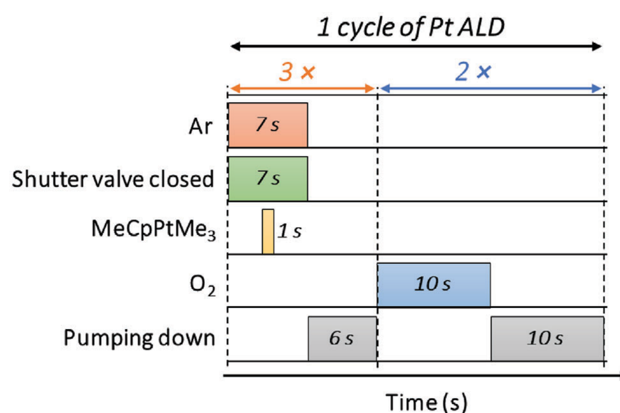

Scheme 1. Schematic representation of 1 Pt ALD cycle.

© 2024 The Authors. Advanced Materials Technologies published by Wiley-VCH GmbH

2365709x, 0, Downloaded from https://onlinelibrary.wiley.com/doi/10.1002/admt.202300878 by University Of Twente Finance Department, Wiley Online Library on [18/01/2024]. See the Terms and Conditions (https://onlinelibrary.wiley.com/terms-and-conditions) on Wiley Online Library for rules of use; OA articles are governed by the applicable Creative Commons License

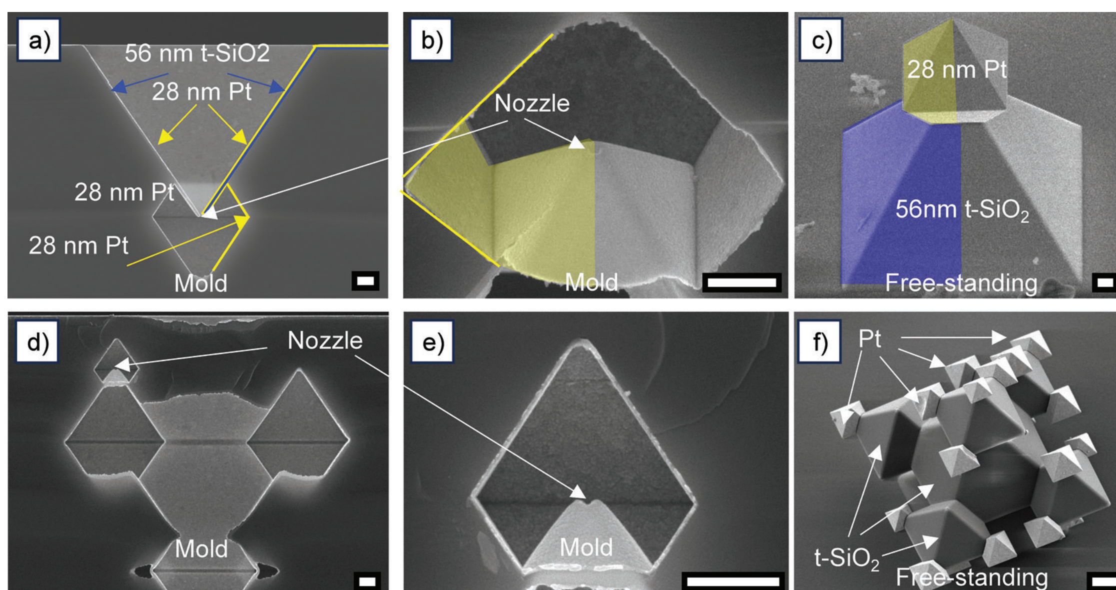

Figure 2. SEM images of 3D Pt molds and free-standing 3D Pt fractal electrodes of increasing complexity. a) Cross-sectional SEM image of a 1st generation mold where the nozzle and ALD deposited Pt are indicated. b) Zoom in at the 1st generation nozzle end, displaying the morphology of the ALD deposited Pt inside the cavity. c) Free-standing 1st generation 3D Pt electrode. d) Cross-sectional SEM image of 3rd generation fractal mold. e) Zoom in at the 3rd generation nozzle end, displaying the morphology of the ALD deposited Pt inside the cavity and around the nozzle. f) Free-standing 3rd generation 3D Pt electrode with exterior Pt octahedra and t-SiO_2 supporting base. Fake color indications have been used in (a–c) to allocate different materials spatially. The scale bars represent 500 nm.

generation cavities. The Pt smoothness is attributed to the Pt growth over {111} faces that terminate the inside of the silicon octahedral mold cavities.

MeCpPtMeHowever, the discussion about the thickness uniformity in the different cavities is broader. The outer Pt octahedra are connected by 25 internal nozzles of t-SiO_2 to the t-SiO_2 base that supports the outer Pt octahedral features. During the Pt-ALD in the 3D mold, the use of the t-SiO_2 nozzles is two-fold. First, as discussed previously, it allows the anisotropic etching of crystalline Si. Second, it also influences the deposition of Pt by ALD into the concave Si cavities.[51] An effect of the nozzle is that it enforces molecular flow dynamics into the Si cavity, considering the dimension of the nozzle and the operating pressure during ALD. Interestingly, this behavior is quite complex, as a Pt deposition on the surface of an outer octahedral cavity in the 3rd generation fractal mold requires the precursor to pass two restrictions and a nozzle before surface deposition. At ALD deposition pressure, the Pt precursor is expected to enter the octahedral crystalline silicon cavity (Figure 1c) and cover the exposed cavity surface. It is important that the pressure within the cavity matches the ALD saturation pressure,[52] which depends on the structure geometry. In this case, it could be expected that a smaller aperture or larger embodiment might reduce precursor intermixing, affecting the Pt deposition rate.[51] An example is given in Figure S3 (Supporting Information), where two different recipes for Pt deposition are used to achieve different deposition regimes. In Figure S3a (Supporting Information), island growth is observed in the 3rd generation octahedral cavity, whereas in Figure S3b (Supporting Information), a film-like deposition is observed. The key change in deposition parameters is the increase in the exposure time of the substrate to the precursor, but also the purge time, to alter both the diffusion of the precursor through the nozzle and the diffusion of the by-products out through the nozzle. The Trimethyl(methylcyclopentadienyl)platinum(IV) ($MeCpPtMe_3$) reacts following a combustion-like reaction, which has been observed in other precursors, producing CO_2 and H_2O after decomposition.[53,54] Deposition of a closed film is key to obtaining a 3D Pt electrode. The way to obtain intact Pt octahedra at the outer octahedral features is if the deposited film is interconnected and conformal (Figure S3b, Supporting Information). Optimally, the deposited film is closed after the Si mold is etched. The observation of the intact octahedra, as imaged in Figure 2c,f, indicates that the film is conformal and closed. The argument for this is two-fold: (1) the SEM images display a closed film, and (2) the selective properties of the wet-chemical etchants toward the material would otherwise have damaged the structures. Sacrificial etching of the mold presented in Figure S3a (Supporting Information) would not yield outer octahedral features.

Figure 3 displays that, in addition to 1st and 3rd, 4th generation 3D electrodes are obtainable. Moreover, the Pt deposition in an array of fractal molds can be translated into 3D Pt electrodes, as presented in Figure 3a. A schematic representation of the 4th generation 3D Pt electrode is shown in Figure 1g. In this case, the supporting base is terminated by 125 octahedra (4th generation, colored in yellow). A similar conclusion can be derived for the actual fabricated structure in Figure 3a. The SEM image in Figure 3a is recorded with a combination of secondary (SE) and backscattered electrons (BSE). The BSE method is sensitive to variations in the elemental atomic number. In this case, the outer octahedra shows up with an intensified signal, indicating a distinct difference in the atomic number of the outer octahedra and the supporting base. A unique feature that deserves attention

© 2024 The Authors. Advanced Materials Technologies published by Wiley-VCH GmbH

2365709x, 0, Downloaded from https://onlinelibrary.wiley.com/doi/10.1002/admt.202300878 by University Of Twente Finance Department, Wiley Online Library on [18/01/2024]. See the Terms and Conditions (https://onlinelibrary.wiley.com/terms-and-conditions) on Wiley Online Library for rules of use; OA articles are governed by the applicable Creative Commons License

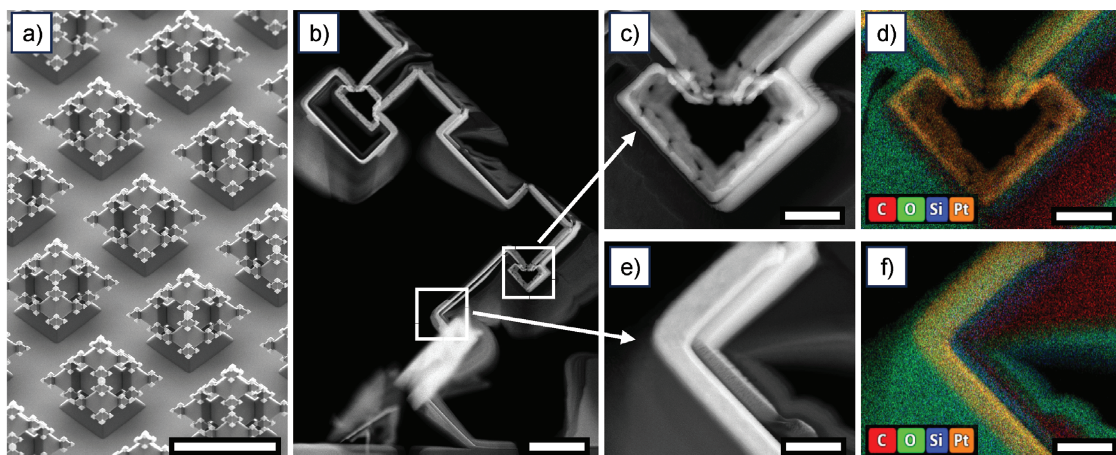

Figure 3. a) Tilted-view of a 4th generation 3D electrode array configured in a hexagonal lattice, the scale bar represents 10 µm. b) STEM-HAADF intersecting a single 4th generation 3D electrode, the scale bar represents 1 µm. c) and e) present enlarged STEM-HAADF images obtained at the 4th generation octahedral feature, (c), and concave corner on the interior of the 2nd generation feature of the supporting base (e). d) and f) display the obtained STEM-EDX mappings for (c) and e), respectively. The remaining scale bars represent 200 nm.

is that some Pt octahedra are 100 nm apart, if not lower. The octahedra separation has recently been shown optically using super-resolution imaging, and the results demonstrate that the octahedra features do not touch each other.[55] Such tight confinement between outer octahedra could have consequences on the fluidic and electric behavior of the contacting electrolyte.

To further investigate the spatial allocation of the materials in the fractal mold, but -more importantly- the 3D Pt electrode, focussed ion beam etching (FIB), scanning transmission electron microscopy (STEM) in high-angular annular dark-field (HAADF), and energy-dispersive X-ray spectroscopy (EDX) mode have been assessed. FIB has been used to prepare a ≈50 nm thick lamella for STEM-HAADF (Figure 3c,e) and STEM-EDX analyses (Figure 3d,f) in two distinct locations. From these measurements, it is observed that, indeed, the Pt film coats conformally along the fractal mold surface. Additionally, it is observed that the Pt:t-SiO_2 phase separation, as schematically presented in Figure 1, is present in the fabricated 3D electrode with t-SiO_2 at the exterior of the supporting base and Pt at the exterior of the outer octahedra. Moreover, it demonstrates that the Pt is interconnected throughout the adjacent octahedral features and nozzles. The results confirm that Pt is present through the entire interior of the 4th generation 3D Pt electrode. At the same time, the outer 125 Pt octahedra can be addressed as a working electrode maintaining the base insulated. Irrespective of the dimensions encountered in a single 3D mold structure, Pt can be deposited uniformly with smaller nozzle and cavity dimensions in higher generations. Later, the Pt inside the 3D mold can be inverted into a free-standing array of 3D Pt electrodes, as evidenced by Figures 2 and 3.

Until now, Pt deposition into 1st, 3rd, and 4th generation 3D Si-molds has been discussed, and the obtention of free-standing structures is exhibited. However, a discussion on the strategy to obtain a free-standing structure is limited to the introduction of the bonding layer in Figure 1e. The ideal scenario is that fractal structures are electrically disconnected by locally back-removing the flat ALD-Pt layer. This step should be accompanied by depositing and patterning a metal layer that selectively connects individual 3D electrodes to a contact pad. This might be interesting for pixelated or interdigitated electrode designs. In this work, the patterning of an electrical interconnect is chosen since electrical contact can be made between the electrolyte and a "dry" contact pad through the interconnects of the 3D electrode.

Additional process steps are conducted to achieve electrical interconnect free-standing structures. The process steps are presented in **Figure 4** and referred to earlier steps in Figure 1e. During ALD, the Pt is deposited uniformly across the substrate into the mold and onto the flat surface, as presented in Figure 1d and Figure 4a. By carrying out ion beam etching (IBE) at a 20° angle to the wafer surface and continuous concentric rotation, a self-shadowing mechanism allows the ALD Pt film to be etched at the flat surface but stay present within the 0th generation pyramidal cavity and higher order octahedral cavities. A schematic representation of the ion beam etching step is shown in Figure 4b. A result is displayed in Figure S4 (Supporting Information), where the entrance to 0th-order pyramidal cavities within the area exposed to the ion beam leads to disconnected (or electrically isolated) cavities.

To fabricate the electrical interconnect, a tri-layer stack consisting of a 5 nm chromium (Cr) adhesion layer, 20 nm Pt, and another 5 nm Cr adhesion layer is sputter-deposited over the entire substrate (Figure 4c). The tri-layer is then patterned by applying, exposing, and developing a positive tone photoresist and sequential IBE under a 45-degree incidence angle relative to the flat substrate surface (Figure 4d). Removing the photoresist layer reveals the patterned tri-layer stack (Figure 4e). Sequentially, a 10 nm thick amorphous silicon layer is sputter-deposited over the entire substrate (Figure 4f). The amorphous silicon facilitates anodic bonding in the areas where the tri-layer stack and/or t-SiO_2 are present. The borosilicate carrier substrate is bonded to the silicon substrate (Figure 4g). After anodic bonding, the Si mold is wet-etched selectively in TMAH, showing the free-standing 3D electrodes that contain an electrical interconnect (Figure 4h,i).

From the fabrication process in Figure 4, a critical design aspect is that the amorphous silicon functions as a sacrificial layer converted into SiO_2 to form the bond between the 3D mold and the carrier substrate using the Cr adhesion layer. Therefore,

© 2024 The Authors. Advanced Materials Technologies published by Wiley-VCH GmbH

2365709x, 0, Downloaded from https://onlinelibrary.wiley.com/doi/10.1002/admt.202300878 by University Of Twente Finance Department, Wiley Online Library on [18/01/2024]. See the Terms and Conditions (https://onlinelibrary.wiley.com/terms-and-conditions) on Wiley Online Library for rules of use; OA articles are governed by the applicable Creative Commons License

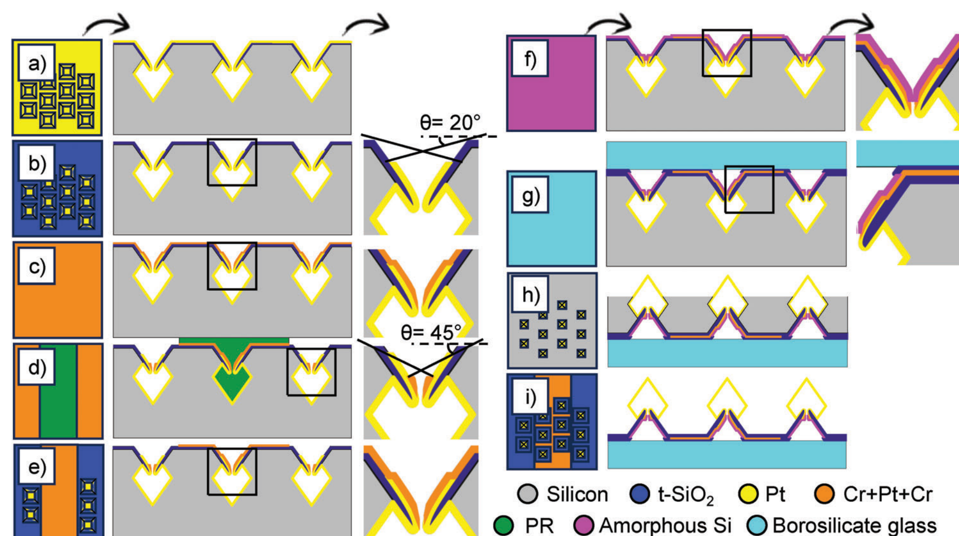

Figure 4. Schematic representation of the back side electrical contact fabrication and wafer bonding. Both top-view and cross-sectional schematics are presented to clarify the individual processing steps. In some process steps, a magnified cross-section version is presented to underline key characteristics. In a), a substrate containing a 3D fractal mold is shown right after the ALD of Pt. In b), IBE is used to partially etch the ALD-deposited Pt from the backside of the substrate using a 20° glancing angle. In c), a tri-layer stack of 5 nm Cr, 20 nm Pt, and 5 nm Cr (Cr+Pt+Cr) is sputter-deposited over the substrate. In d), a positive tone photoresist (PR) layer is patterned to mask the tri-layer stack, followed by ion beam etching at 45° to pattern the tri-layer stack. In e), the PR layer is stripped, revealing the patterned Cr+Pt+Cr layer. In f), the sputter-deposition of a 10 nm thick amorphous silicon film is carried out. In g), anodic bonding of the structure is performed where the silicon substrate containing the patterned fractal structure is bonded to a borosilicate glass substrate. The amorphous silicon layer is fully converted to t-SiO_2 at the bonding interface. In h,i), the removal of the silicon substrate by wet chemical etching is presented. The dashed boxes indicate the area where the corresponding magnified schematic is presented. A color legend indicates the different materials.

the thickness of the sputter-deposited amorphous silicon layer is essential. If the layer is too thin, it can result in a poor bond, while a too-thick layer can create an electric leakage path. During the anodic bonding process, one should ensure that the amorphous silicon is fully converted into SiO_2. Therefore, experiments have been conducted to characterize the oxidation behavior of sputter-deposited amorphous silicon during anodic bonding. The results are presented in Figure S5 (Supporting Information). It is observed that a 10 nm amorphous silicon layer is fully converted into SiO_2. A 20 nm or thicker sputter-deposited amorphous silicon layer is not fully converted into SiO_2.

Another design aspect regards the choice of materials for forming the tri-layer stack. First, the materials in the tri-layer stack should be compatible with anodic bonding at the stated temperature, i.e., the material should be anodically bondable to glass under these conditions and should not disintegrate. Second, the materials should withstand the etchant to remove the silicon wafer to obtain the final free-standing patterned and electrically connected fractal. To connect the electrical interfacing to the 3D Pt electrodes, openings in the borosilicate glass wafer can be in place before the bonding to enable electrical connection to the patterned fractal footprints, as shown in Figure S6 (Supporting Information). This step allows the 3D Pt fractals to be in contact with chemical environments while maintaining electrical connections unexposed.

In summary, the novelty of this work relies not only on the fabrication of fractal-like structures but also on fabrication control over the location of the Pt octahedral features. It also showcases the establishment of an electrical interconnect across the Pt octahedra supported over the fractal network, which is not trivial for 3D Pt electrodes.

2.2. Pt Octahedra for Electrochemical Sensing Under Fouling Environments

The electrochemical functionality of the Pt octahedra spatially distributed over the 4th generation geometry (Figure 3) is demonstrated during electrochemical sensing of 2 mM $K_3Fe(CN)_6$ in a biofouling environment with *P. aeruginosa*. Prior to the experiments with *P. aeruginosa*, 3D electrodes, and flat electrodes are assessed electrochemically in a solution of 0.1 M KCl and 2 mM ferrocyanide ($K_3[Fe(CN)_6]$) in PBS and another measurement 24 h after adding 10 mg mL^{-1} BSA as shown in Figures S7–S10 (Supporting Information). In this case, the cyclic voltammetry (CV) scans for $K_3Fe(CN)_6$ show the redox characteristics of the ferrocyanide/ferricyanide couple.[54] The redox reaction is presented in Equation (1), where ferrocyanide/ferricyanide reduction occurs via single electron transfer. The proposed reaction can be used as a guideline when assessing the CV in the presence of *P. aeruginosa* (**Figure 5**) and other molecular biofouling agents (Figures S7–S10, Supporting Information).

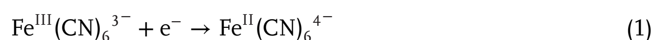

$$Fe^{III}(CN)_6{}^{3-} + e^- \rightarrow Fe^{II}(CN)_6{}^{4-} \quad (1)$$

The electrochemical assessment with $K_3[Fe(CN)_6]$ in Figure S7 (Supporting Information) shows reaction reversibility for the flat and 3D electrodes. Figure S7 (Supporting Information) results are analyzed using the Randles-Sevcik approach in

© 2024 The Authors. Advanced Materials Technologies published by Wiley-VCH GmbH

2365709x, 0, Downloaded from https://onlinelibrary.wiley.com/doi/10.1002/admt.202300878 by University Of Twente Finance Department, Wiley Online Library on [18/01/2024]. See the Terms and Conditions (https://onlinelibrary.wiley.com/terms-and-conditions) on Wiley Online Library for rules of use; OA articles are governed by the applicable Creative Commons License

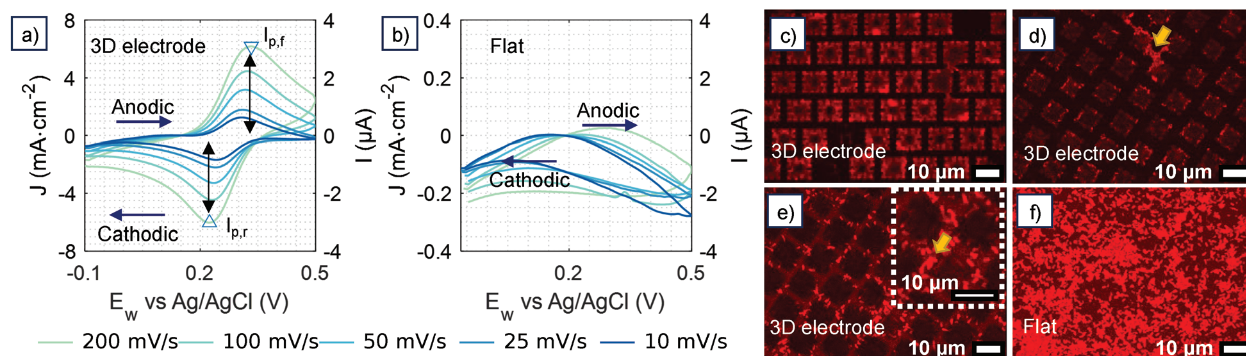

Figure 5. Cyclic voltammetry scans of Pt octahedra in the presence of *P. aeruginosa* and $K_3[Fe(CN)_6$ for a) Pt octahedra and b) Pt flat. c–f) Confocal images for *P. aeruginosa* over Pt octahedra and f) over Pt-coated flat substrate. The inset in e) highlights *P. aeruginosa* with a rod-like shape.

Figure S8 (Supporting Information) to gain information about reaction reversibility.[56] Deviation from a linear trend in the Randles-Sevick plot typically indicates the irreversibility or quasi-reversibility inherent to the system. Figure S8 (Supporting Information) analysis suggests a slightly non-linear behavior, which can be due to deviation from an ideal reversible process. Similarly, quasi-reversible behavior has been observed for the 3D electrodes in contact with *P. aeruginosa* (Figure 5). The attributions are supplemented further by comparing the ratio between the cathodic ($i_{p,f}$) and anodic ($i_{p,r}$) currents. For quasi-reversible reactions, the ratio between $i_{p,f}$ and $i_{p,r}$ should be close to unity. In our case, the ratio is close to 0.7 at 200 mV/s for Pt octahedra, while we cannot determine for Pt flat due to the general absence of prominent peaks, as observed in Figure 5. Other criteria to define a quasi-reversible system are the peak potential (E_p), which should be scan rate dependent, and the cathodic and anodic peak potential difference (ΔE_p), expected to increase with the scan rate.[57] For anodic Ep (E_{pa}) and cathodic Ep (E_{pc}), the electrochemical potential increases as a function of the scan rate from 0.02 and 0.01, while the ΔE_p changes from 0.09 to 0.08. Therefore, it is safe to assume that it is a quasi-reversible behavior.

Furthermore, a reduction in surface area has been observed to be more pronounced for the flat than the 3D electrode, demonstrating the relevancy of spatial patterning. This fact becomes evident when comparing the difference in electrode surface area before and after 24 h BSA. In this case, BSA has been selected as a biofouling molecule of known concentration (i.e., 10 mg/mL) in the electrolyte. Differences between before and after BSA addition show a reduction in the active electrode surface area (ΔA_{eff}) ˜49 ± 7% for the flat electrode. In contrast, a 25% ± 2% reduction in ΔA_{eff} for the 3D electrode has been found, as shown in Tables S1 and S2 (Supporting Information). The results are accompanied by a 24% ± 16% decrease in peak current for the flat substrate and a 14% ± 5% decrease in peak current for the 3D electrode 24 h after adding BSA.

We further investigate the 3D electrode charge transfer, kinetic, and mass transport behavior using potentiometric electrochemical impedance spectroscopic (PEIS) shown in Figures S9 and S10 and Table S3 (Supporting Information), which seem unaffected by the presence of BSA. Although the latest kinetics and transport processes are unaffected for the 3D electrode, PEIS results in Table S3 (Supporting Information) show a relatively large resistive component due to a film resistance imposed by the ALD-deposited Pt. This means that the current path may reach from the contact pad through the entire ALD-Pt film, covering the inside of the 4th fractal generation that conforms to the 3D electrode (Figures 2–4). The results from the 3D electrode differ from the flat electrode, where an increase in charge transfer resistance and Warburg impedance is observed (Figures S9 and S10 and Table S3, Supporting Information).

The Pt octahedra and flat film are also characterized in 0.1 M H_2SO_4 (Figures S11 and S12, Supporting Information). The measured CVs in the presence of 0.1 M H_2SO_4 show that multiple hydrogen adsorption, desorption, and oxide formation and reduction peaks are observed, matching those observed in other Pt electrochemical systems.[58] The peaks are prominent in the spectra measured with the 3D electrode. Assuming that, in the absence of geometrical differences, the electrochemical systems are similar, i.e., the same electrolyte and the same electrode material, the electrode geometry may play a role in mass transport and the reaction kinetics. Any changes in this may relate to the process at the edges and corners of the octahedra due to electric field effects.

The 3D electrode PEIS measurements in Figures S11 and S12 (Supporting Information) carried out in 0.1 M H_2SO_4 are conducted with a 10 mV AC modulation on a 0.5 V DC potential versus Ag/AgCl, meaning that the PEIS collection occurred in the double layer formation regime initially shows strong capacitive behavior at low frequencies, similar to the flat electrode. However, the 3D electrode transitions to a kinetic-limited regime at higher frequencies due to its unique 3D characteristics, which affect the diffusion layers and charge transfer dynamics. This means that at low frequencies, the 3D electrode behaves like a planar film, but as frequency increases, the contributions to the double layer become more significant, influencing the redistribution of ions and charge transfer dynamics. From the electrochemical analyses, the 3D electrode shows a more stable operation under various electrochemical environments. Therefore, its functionality is assessed in more complex biofouling conditions, such as in the presence of *P. aeruginosa* in Figure 5.

The CVs recorded on the flat and 3D electrodes depicted in Figure 5a,b shows the redox characteristics of the ferrocyanide/ferricyanide couple on the 3D electrode (Figure 5a) but barely in the case of the flat electrode (Figure 5b). Insights into such electrochemical behavior are then generated using confocal microscopy images to establish why fundamentally different CVs

© 2024 The Authors. Advanced Materials Technologies published by Wiley-VCH GmbH

2365709x, 0, Downloaded from https://onlinelibrary.wiley.com/doi/10.1002/admt.202300878 by University Of Twente Finance Department, Wiley Online Library on [18/01/2024]. See the Terms and Conditions (https://onlinelibrary.wiley.com/terms-and-conditions) on Wiley Online Library for rules of use; OA articles are governed by the applicable Creative Commons License

are found over the 3D and flat electrode surface in the presence of *P. aeruginosa*. Figure 5c–f shows a confocal image of *P. aeruginosa* over the 3D electrode with a fractal-like structure where the biofilm and bacteria are stained with crystal violet and revealed in red. Figure 5c,d shows the presence of the fractals outlined in red. This is attributed to *P. aeruginosa* and biofilm attached to the 3D electrode with octahedral features, probably within the small apertures of no larger than 200 nm.[59] Similar bacterial cell behavior has been shown over nanostructured surfaces, leading to a change in bacteria organization over structured surfaces.[60–63] In Figure 5e, an additional confocal image of the bottom part of the Pt octahedra shows only a few *P. aeruginosa* allocated between the groves, i.e., fractal structure-to-fractal structure interspace (see inset with the yellow arrow). The results contrast with a flat substrate coated with Pt in Figure 5f, where the surface of the flat electrode is completely covered.

Combining electrochemical measurements using $K_3Fe(CN)_6$ for Pt octahedra (Figure 5a) and Pt flat (Figure 5b) with confocal microscopy images in Figure 5c–f, we deduce that *P. aeruginosa* obstructs the surfaces of Pt octahedra and flat electrodes. No electrochemical signal for $K_3Fe(CN)_6$ is detected for Pt flat, while Pt octahedra exhibited signals. Deviations from reversibility in the electrochemical signal are also observed, attributed to surface blockage by bacteria and biomolecules during biofilm growth. Altogether, the results highlight the advantage of structured Pt octahedra. Our attributions are in conjunction with Figures S7–S12 and Tables S1–S3 (Supporting Information), from where we conclude that the 3D electrode demonstrates more stable operation under biofouling conditions.

3. Conclusions

A fabrication method to obtain a 3D fractal-like Pt electrode array has been reported. The 3D electrode contains Pt octahedra supported by an insulating t-SiO_2 base. The 125 Pt octahedra that functioned as the working electrode has been successfully electrically connected through the interior of the electrode. As proof of concept, electrochemical sensing of ferrocyanide in a biofouling environment is assessed using *P. aeruginosa*. Confocal microscopy images revealed that the fractal structures of the 3D electrode are partially covered with *P. aeruginosa*. This behavior is consistent with findings on structured surfaces, which contrasts with the complete coverage of the flat electrode. The electrochemical measurements in the presence of *P. aeruginosa* using ferrocyanide indicate that the 3D electrode retained electrochemical signals, while the flat electrode did not. Although deviations from reversibility are observed in the electrochemical signals, the 3D electrode demonstrated more stable operation than its flat counterpart under biofouling conditions (BSA and *P. aeruginosa*).

4. Experimental Section

Atomic Layer Deposition of Pt: Pt was deposited into the negative silicon replica using atomic layer deposition (ALD). The deposition of Pt was carried out using a home-built ALD reactor already described elsewhere.[64] The pumping system of the ALD reactor consisted of a turbopump connected to a rotary pump, keeping the pressure of the reactor chamber close to 10^{-6} mbar. A shutter valve allowed the reactor to be isolated from the pumping system. The chamber walls were heated to 90°C, while the temperature of the substrate holder was maintained at 300 °C. The reactor was equipped with an inductively coupled plasma source (ICP), used for the plasma cleaning of the substrate before each deposition. The plasma cleaning procedure was carried out using flowing O_2 gas (>99.999% purity) at the pressure of 7.5×10^{-2} mbar, and the plasma was then ignited for 15 min at the power of 100 W.

Trimethyl(methylcyclopentadienyl)platinum(IV) ($MeCpPtMe_3$, 98% purity) was used as a precursor. The $MeCpPtMe_3$ was placed in a stainless-steel cylindrical bubbler heated to 40°C. Argon gas (>99.999% purity) was used to carry the $MeCpPtMe_3$ vapor from the bubbler to the reactor through a line heated at 60 °C. O_2 gas at the pressure of 1.0 mbar was used as a reactant.

For the conformal deposition of platinum into the fractal structure (Scheme 1), $MeCpPtMe_3$ pulses were performed while keeping the shutter valve between the reactor and the pumping system closed. The rationale was to keep the precursor confined in the chamber as long as possible to let it diffuse inside the fractal structure. The ALD cycle started by flowing Ar to stabilize the gas flow for 7 s while closing the shutter valve (7 s). Then, $MeCpPtMe_3$ was dosed for 1 s by diverting the Ar flow from the line to the precursor's cylinder. Then, the Ar flow was diverted back for 3 s to purge the line. After purging the line, the shutter valve was opened for 6 s to pump down the reactor. These steps were repeated 3 times. Subsequently, within the same ALD cycle, the O_2 dosing was performed for 10 s followed by 10 s of pumping down. The O_2 reactant step was repeated two times. The whole ALD cycle was repeated 400 times to achieve ca. 25 ± 5 nm layer thickness of Pt over the silicon mold (Figure 1).

Electrochemical Measurements: *Activation of the 3D Pt electrodes*: The electrochemical measurements were carried out in a three-electrode configuration. Pt octahedra are used as the working electrode. The Pt octahedra for the geometrical area with 0.0018 cm^2 are considered. Pt flat was used as a working electrode control. Pt has a 0.01 cm^2 geometrical area. The measurements were carried out with potentio-static/dynamic electrochemical techniques with potentiostat/galvanostat/zero resistance ammeter. A Pt coil was used as a counter electrode, and Ag/AgCl was used as the reference electrode. In all cases, 0.1 M H_2SO_4 (98% purity) was used to activate the Pt surface. The cyclic voltammogram of Pt octahedra is shown in the supporting information.

Biofilm Formation: *P. aeruginosa* (PAO1 / ATCC 27 853) cultures were grown overnight (200 rpm, at 37 °C) in LB medium (Luria Broth). The bacterial cell concentration was adjusted to 0.1 OD_{600nm} in sterile Minimal medium M63 ($(NH_4)_2SO_4$ 15 mm KH_2PO_4/K_2HPO_4 22 mm/40 mm, $FeSO_4$ 1.7 µm) supplemented with 1 mm $MgSO_4$, 0.4% (w/v) arginine and 2 mm $K_3[Fe(CN)_6]$. These chemicals were purchased with purities higher than 98%. Before microbiological assays, the working electrodes were placed in 6-well cell culture plates and sterilized under UV light for 1 h. Each substrate was immersed in 8.5 mL of bacterial cell suspension and incubated at 37 °C for 48 h. After 48 h, biofilm was formed.[65] The biofilm at the interface was carefully removed using a pipette tip; then, the surfaces were washed 3 times with purified water type one with water resistivity close to 18 MΩ cm.

The working electrodes containing *P. aeruginosa* biofilm were placed in 2 mM $K_3Fe(CN)_6$ in 0.1 M KCL and 0.1 M KH_2PO_4. These chemicals were purchased with purities higher than 98%. CV scans were conducted with scanning rates varying between 10 and 200 mV s^{-1}. Before imaging, *P. aeruginosa* was stained with crystal violet. After staining, surfaces were rinsed with sterile, purified water type one with water resistivity ≈18 MΩ cm^{-1} and immediately analyzed using a confocal microscope.

Scanning Electron Microscopy: SEM images of Pt octahedra supported over fractal-like structures were taken using an SEM microscope operated at 2 kV coupled with a High-Efficiency Secondary Electron Detector.

Statistical Analysis: To calculate the values of $i_{p,f,}$ and $i_{p,r}$, CV data sets were normalized to facilitate experiment comparisons. The normalization procedure utilized the slope derived from the double-layer capacitance within the 0.10 to 0.15 V range for CVs recorded in the presence of 2 mM $K_3Fe(CN)_6$. From this slope, a linear baseline was calculated and subtracted from the CV data for each scan rate. The peaks were established relative to the normalized (baseline-corrected) dataset. The presented mean

© 2024 The Authors. Advanced Materials Technologies published by Wiley-VCH GmbH

2365709x, 0, Downloaded from https://onlinelibrary.wiley.com/doi/10.1002/admt.202300878 by University Of Twente Finance Department, Wiley Online Library on [18/01/2024]. See the Terms and Conditions (https://onlinelibrary.wiley.com/terms-and-conditions) on Wiley Online Library for rules of use; OA articles are governed by the applicable Creative Commons License

values of $i_{p,f,}$ and $i_{p,r}$ and the standard deviation are based on measuring five peak values and an average of three cycles for every scan rate. Additional information is found in the supporting information. A least-squares linear regression approach to analyze ΔA_{eff} values and their corresponding confidence intervals is employed to determine the regression coefficients representing the slope and intercept. The Randles-Sevcik equation facilitated the calculation of ΔA_{eff} based on the fitted slope. Subsequently, standard errors were computed, and the degrees of freedom were established at three. To ascertain the precision of our parameter estimates, critical values from the two-sided t-distribution were derived, guided by the desired confidence level and degrees of freedom. The corresponding critical t-value was used at a 95% confidence level with three degrees of freedom to delineate a range in the true slope and intercept values and thus ΔA_{eff}. All statistical calculations were performed in Matlab.

Supporting Information

Supporting Information is available from the Wiley Online Library or from the author.

Acknowledgements

D.J. and C.E. contributed equally to this work. C.E., A.S.-A., and H.G. were recipients of the Horizon 2020 ERC research and innovation program of the European Union funding under Grant Agreement No. 742004. The authors thank M. J. Goodwin and M. Tsvetanova for their assistance during sample FIB preparation and TEM analysis. The authors acknowledge A. Raman and R. Espinosa-Flores for scientific discussions, which are instrumental to this work.

Conflict of Interest

A.S.-A., D.J., C.E., E.J.W.B., and N.T., filed a commercial patent for using topographic surfaces as cell growth substrates. The following patents have been filed resulting from the work reported in this manuscript: PCT/NL2022/050769. A.S.-A., E.J.W.B., N.T., and S.K. are co-founders of Encytos B.V.

Data Availability Statement

The data that support the findings of this study are available from the corresponding author upon reasonable request.

Keywords

3D electrodes, electrochemistry, fabrication, platinum, sensing

Received: May 30, 2023
Revised: December 22, 2023
Published online:

[1] J.-H. Lee, J. P. Singer, E. L. Thomas, *Adv. Mater.* **2012**, *24*, 4782.
[2] D. Jonker, Z. Jafari, J. P. Winczewski, C. Eyovge, J. W. Berenschot, N. R. Tas, J. G. E. Gardeniers, I. De Leon, A. Susarrey-Arce, *Nanoscale Adv* **2021**, *3*, 4926.
[3] J. Winczewski, M. Herrera, C. Cabriel, I. Izeddin, S. Gabel, B. Merle, A. Susarrey Arce, H. Gardeniers, *Adv. Opt. Mater.* **2022**, *10*, 2102758.
[4] J. Winczewski, M. Herrera, H. Gardeniers, A. Susarrey-Arce, *Chem. Commun.* **2023**, *59*, 3095.
[5] S. J. P. Callens, C. H. Arns, A. Kuliesh, A. A. Zadpoor, *Adv. Funct. Mater.* **2021**, *31*, 2101373.
[6] M. Centonze, E. Berenschot, S. Serrati, A. Susarrey-Arce, S. Krol, *Pharmaceutics* **2022**, *14*, 218.
[7] F. Dituri, M. Centonze, E. J. W. Berenschot, N. R. Tas, A. Susarrey-Arce, S. Krol, *Nanomaterials* **2021**, *11*, 3233.
[8] N. E. Putra, K. G. N. Borg, P. J. Diaz-Payno, M. A. Leeflang, M. Klimopoulou, P. Taheri, J. M. C. Mol, L. E. Fratila-Apachitei, Z. Huan, J. Chang, J. Zhou, A. A. Zadpoor, *Acta Biomater.* **2022**, *148*, 355.
[9] S. C. Carrara, A. Davila-Lezama, C. Cabriel, E. J. W. Berenschot, S. Krol, J. G. E. Gardeniers, I. Izeddin, H. Kolmar, A. Susarrey-Arce, *Mater Today Bio* **2024**, *24*, 100897.
[10] J. Zhao, H. Lu, X. Zhao, O. I. Malyi, J. Peng, C. Lu, X. Li, Y. Zhang, Z. Zeng, G. Xing, Y. Tang, *ACS Mater. Lett.* **2020**, *2*, 1041.
[11] V. Egorov, U. Gulzar, Y. Zhang, S. Breen, C. O'dwyer, *Adv. Mater.* **2020**, *32*, 2000556.
[12] X. Tian, K. Zhou, *Nanoscale* **2020**, *12*, 7416.
[13] L. Borasi, S. Frasca, K. Nicolet-Dit-Felix, E. Charbon, A. Mortensen, *Appl. Mater. Today* **2022**, *29*, 101647.
[14] D. J. Beesley, J. Semple, L. Krishnan Jagadamma, A. Amassian, M. A. Mclachlan, T. D. Anthopoulos, J. C. Demello, *Nat. Commun.* **2014**, *5*, 3933.
[15] J. P. Winczewski, S. Zeiler, S. Gabel, A. Susarrey-Arce, J. G. E. Gardeniers, B. Merle, *Mater. Des.* **2023**, *232*, 112142.
[16] J. P. Winczewski, J. A. Dávila, M. Herrera-Zaldívar, F. Ruiz-Zepeda, R. M. Córdova-Castr, C. R. P. de la Vega, C. Cabriel, I. Izeddin, J. G. E. Gardeniers, A. Susarrey-Arce, *Adv. Mater.* **2023**, 2307077.
[17] F. Mayer, S. Richter, J. Westhauser, E. Blasco, C. Barner-Kowollik, M. Wegener, *Sci. Adv.* **2019**, *5*, 9160.
[18] X. Peng, L. Yue, S. Liang, S. Montgomery, C. Lu, C.-M. Cheng, R. Beyah, R. R. Zhao, H. J. Qi, *Adv. Funct. Mater.* **2022**, *32*, 2112329.
[19] S. K. Seol, D. Kim, S. Lee, J. H. Kim, W. S. Chang, J. T. Kim, *Small* **2015**, *11*, 3896.
[20] L. Hirt, S. Ihle, Z. Pan, L. Dorwling-Carter, A. Reiser, J. M. Wheeler, R. Spolenak, J. Vörös, T. Zambelli, *Adv. Mater.* **2016**, *28*, 2311.
[21] C. A. R. Chapman, H. Chen, M. Stamou, J. Biener, M. M. Biener, P. J. Lein, E. Seker, *ACS Appl. Mater. Interfaces* **2015**, *7*, 7093.
[22] I. R. Minev, N. Wenger, G. Courtine, S. P. Lacour, *APL Mater.* **2015**, *3*, 014701.
[23] P. Daggumati, Z. Matharu, L. Wang, E. Seker, *Anal. Chem.* **2015**, *87*, 8618.
[24] D. Xia, S. R. J. Brueck, *Nano Lett.* **2004**, *4*, 1295.
[25] G. Wyatt-Moon, D. G. Georgiadou, J. Semple, T. D. Anthopoulos, *ACS Appl. Mater. Interfaces* **2017**, *9*, 41965.
[26] B. Rezaei, S. Saghir, J. Y. Pan, R. S. Davidsen, S. S. Keller, *Micromachines* **2022**, *13*, 371.
[27] H. Masuda, K. Fukuda, *Science* **1979**, *268*, 1466.
[28] A. Hai, J. Shappir, M. E. Spira, *Nat. Methods* **2010**, *7*, 200.
[29] E. Seker, Y. Berdichevsky, M. R. Begley, M. L. Reed, K. J. Staley, M. L. Yarmush, *Nanotechnology* **2010**, *21*, 125504.
[30] M. R. Abidian, D. C. Martin, *Adv. Funct. Mater.* **2009**, *19*, 573.
[31] J. Patel, L. Radhakrishnan, B. Zhao, B. Uppalapati, R. C. Daniels, K. R. Ward, M. M. Collinson, *Anal. Chem.* **2013**, *85*, 11610.
[32] E. E. Krommenhoek, J. G. E. Gardeniers, J. G. Bomer, A. Van Den Berg, X. Li, M. Ottens, L. A. M. Van Der Wielen, G. W. K. Van Dedem, M. Van Leeuwen, W. M. Van Gulik, J. J. Heijnen, *Sens Actuators B Chem* **2006**, *115*, 384.
[33] E. E. Krommenhoek, J. G. E. Gardeniers, J. G. Bomer, X. Li, M. Ottens, G. W. K. Van Dedem, M. Van Leeuwen, W. M. Van Gulik, L. A. M. Van Der Wielen, J. J. Heijnen, A. A. Van Den Berg, *Anal. Chem.* **2007**, *79*, 5567.
[34] Y. Liu, X. Li, J. Chen, C. Yuan, *Front Chem* **2020**, *8*, 1102.
[35] X. Chen, T. Li, J. Shen, Z. Hu, *Chemom. Intell. Lab. Syst.* **2016**, *155*, 19.
[36] A. Hasan, A. Paul, N. E. Vrana, X. Zhao, A. Memic, Y.-S. Hwang, M. R. Dokmeci, A. Khademhosseini, *Biomaterials* **2014**, *35*, 7308.

© 2024 The Authors. Advanced Materials Technologies published by Wiley-VCH GmbH

2365709x, 0, Downloaded from https://onlinelibrary.wiley.com/doi/10.1002/admt.202300878 by University Of Twente Finance Department, Wiley Online Library on [18/01/2024]. See the Terms and Conditions (https://onlinelibrary.wiley.com/terms-and-conditions) on Wiley Online Library for rules of use; OA articles are governed by the applicable Creative Commons License

[37] H. Kai, R. Toyosato, M. Nishizawa, *RSC Adv.* **2018**, *8*, 15985.
[38] M. Marxen, R. M. Henkelman, *Am. J. Physiol.: Heart Circ. Physiol.* **2003**, *284*, H1848.
[39] A. Díaz Lantada, B. Pareja Sánchez, C. Gómez Murillo, J. Urbieta Sotillo, *Expert Rev. Med. Devices* **2013**, *10*, 629.
[40] G. Wang, Y. Gu, L. Zhao, J. Xuan, G. Zeng, Z. Tang, Y. Sun, *Chem. Eng. Sci.* **2019**, *195*, 250.
[41] Y. De Rancourt De Mimérand, K. Li, J. Guo, *ACS Appl. Mater. Interfaces* **2019**, *11*, 24771.
[42] Y. D. R. De Mimérand, K. Li, C. Zhou, X. Jin, X. Hu, Y. Chen, J. Guo, *ACS Appl. Mater. Interfaces* **2020**, *12*, 43138.
[43] L. Lei, D. Wang, Y. Kang, Y. De Rancourt De Mimérand, X. Jin, J. Guo, *ACS Appl. Mater. Interfaces* **2022**, *14*, 11820.
[44] M. Lafuente, E. Berenschot, R. Tiggelaar, R. Mallada, N. Tas, M. Pina, *Micromachines* **2018**, *9*, 60.
[45] Z. Zhu, N. Wei, B. Yan, B. Shen, J. Gao, S. Sun, H. Xie, H. Xiong, C. Zhang, R. Zhang, W. Qian, S. Fu, L. Peng, F. Wei, *ACS Nano* **2021**, *15*, 5129.
[46] J. Warner, P. Soman, W. Zhu, M. Tom, S. Chen, *ACS Biomater. Sci. Eng.* **2016**, *2*, 1763.
[47] S. Galarza, A. J. Crosby, C. Pak, S. R. Peyton, *Adv. Healthcare Mater.* **2020**, *9*, 1901419.
[48] A. Weightman, S. Jenkins, M. Pickard, D. Chari, Y. Yang, *Nanomedicine* **2014**, *10*, 291.
[49] J. W. Berenschot, R. M. Tiggelaar, J. Geerlings, J. G. E. Gardeniers, N. R. Tas, M. Malankowska, M. P. Pina, R. Mallada, *Sympos. on Design, Test, Integration and Packaging of MEMS/MOEMS*, IEEE, New York City **2016**, *2016*, 3.
[50] E. J. W. Berenschot, H. V. Jansen, N. R. Tas, *J. Micromech. Microeng.* **2013**, *23*, 055024.
[51] H. C. M. Knoops, A. J. M. Mackus, M. E. Donders, M. C. M. Van De Sanden, P. H. L. Notten, W. M. M. Kessels, *Electrochem. Solid-State Lett.* **2009**, *12*, G34.
[52] D. Pan, T.-C. Jen, C. Yuan, *Int. J. Heat Mass Transf.* **2016**, *96*, 189.
[53] J. Arriaga Dávila, J. P. Winczewski, M. Herrera-Zaldívar, E. A. Murillo-Bracamontes, C. Rosero Arias, N. Pineda-Aguilar, J. L. Cholula-Díaz, I. De Leon, H. Gardeniers, A. Susarrey Arce, E. Martínez-Guerra, *Appl. Surf. Sci.* **2023**, *636*, 157796.
[54] A. J. M. Mackus, N. Leick, L. Baker, W. M. M. Kessels, *Chem. Mater.* **2012**, *24*, 1752.
[55] C. Cabriel, R. M. Córdova-Castro, E. Berenschot, A. Dávila-Lezama, K. Pondman, S. L. Gac, N. Tas, A. Susarrey-Arce, I. Izeddin, *bioRxiv* **2023**, 2023.11.07.566090.
[56] S. Mousavihashemi, S. Murcia-López, M. A. Rodriguez-Olguin, H. Gardeniers, T. Andreu, J. R. Morante, A. Susarrey Arce, C. Flox, *ChemCatChem* **2022**, *14*, 202201106.
[57] H. Wang, S. Y. Sayed, E. J. Luber, B. C. Olsen, S. M. Shirurkar, S. Venkatakrishnan, U. M. Tefashe, A. K. Farquhar, E. S. Smotkin, R. L. Mccreery, J. M. Buriak, *ACS Nano* **2020**, *14*, 2575.
[58] Y. Sugawara, T. Okayasu, A. P. Yadav, A. Nishikata, T. Tsuru, *J. Electrochem. Soc.* **2012**, *159*, F779.
[59] A. Susarrey-Arce, I. Sorzabal-Bellido, A. Oknianska, F. Mcbride, A. J. Beckett, J. G. E. Gardeniers, R. Raval, R. M. Tiggelaar, Y. A. Diaz Fernandez, *J. Mater. Chem. B* **2016**, *4*, 3104.
[60] A. Susarrey-Arce, J. F. Hernández-Sánchez, M. Marcello, Y. Diaz-Fernandez, A. Oknianska, I. Sorzabal-Bellido, R. Tiggelaar, D. Lohse, H. Gardeniers, J. Snoeijer, A. Marin, R. Raval, *ACS Appl Bio Mater* **2018**, *1*, 1294.
[61] A. Susarrey-Arce, A. Marin, A. Massey, A. Oknianska, Y. Díaz-Fernandez, J. F. Hernández-Sánchez, E. Griffiths, J. G. E. Gardeniers, J. H. Snoeijer, D. Lohse, R. Raval, *Langmuir* **2016**, *32*, 7159.
[62] I. Sorzabal-Bellido, L. Barbieri, A. J. Beckett, I. A. Prior, A. Susarrey-Arce, R. M. Tiggelaar, J. Fothergill, R. Raval, Y. A. Diaz Fernandez, *Nanomaterials* **2022**, *12*, 683.
[63] A. Uneputty, A. Dávila-Lezama, D. Garibo, A. Oknianska, N. Bogdanchikova, J. F. Hernández-Sánchez, A. Susarrey-Arce, *Coll. Interf. Sci. Commun.* **2022**, *46*, 100560.
[64] Y. Hajar, V. Di Palma, V. Kyriakou, M. A. Verheijen, E. A. Baranova, P. Vernoux, W. M. M. Kessels, M. Creatore, M. C. M. Van De Sanden, M. N. Tsampas, *Electrochem. Commun.* **2017**, *84*, 40.
[65] S. P. Bernier, D.-G. Ha, W. Khan, J. H. Merritt, G. A. O'toole, *Res Microbiol* **2011**, *162*, 680.

© 2024 The Authors. Advanced Materials Technologies published by Wiley-VCH GmbH

2365709x, 0, Downloaded from https://onlinelibrary.wiley.com/doi/10.1002/admt.202300878 by University Of Twente Finance Department, Wiley Online Library on [18/01/2024]. See the Terms and Conditions (https://onlinelibrary.wiley.com/terms-and-conditions) on Wiley Online Library for rules of use; OA articles are governed by the applicable Creative Commons License